

Capillary condensation for fluids in spherical cavities

Ignacio Urrutia^{1,†} and Leszek Szybisz^{1,2,*}

¹*Laboratorio TANDAR, Departamento de Física, Comisión Nacional de Energía Atómica,
Av. del Libertador 8250, RA-1429 Buenos Aires, Argentina*

²*Departamento de Física, Facultad de Ciencias Exactas y Naturales,
Universidad de Buenos Aires, Ciudad Universitaria, RA-1428 Buenos Aires, Argentina*

(November 16, 2018)

The capillary condensation for fluids into spherical nanocavities is analyzed within the frame of two theoretical approaches. One description is based on a widely used simplified version of the droplet model formulated for studying atomic nuclei. The other, is a more elaborated calculation performed by applying a density functional theory. The agreement between both models is examined and it is shown that a small correction to the simple fluid model improves the predictions. A connection to results previously obtained for planar slits and cylindrical pores is done.

FILENAME: cavity1.tex

PACS numbers: 61.20.-p, 64.70.-p, 67.70.+n

I. INTRODUCTION

Since more than a decade a so called simple fluid model (SFM) is being applied for analyzing wetting properties of classical and quantum fluids adsorbed onto planar substrates [1,2]. The chief idea of this description is to write down the free energy of the adsorbate as a sum of dominant volume, surface, and substrate terms. As shown in Refs. [3] and [4], the use of this SFM for studying capillary condensation in the case of adsorption between two parallel planar walls (i.e. in a slit geometry) yields a rich pattern of phase transitions in agreement with more elaborated calculations carried out with density functional (DF) approaches. More recently, the SFM has been extended to investigate systems with cylindrical symmetry [5–9]. The authors of Ref. [7] have found that for a rather compact regular array of infinitely long, solid, and parallel cylinders, besides the well known film and capillary condensation (CC) phases, an additional necking configuration may appear. On the other hand, in Ref. [8] we have applied this SFM to describe CC transitions of noble gases confined into single cylindrical pores of alkali metals finding a nearly universal behavior. A detailed comparison of SFM and DF results performed in Ref. [9] indicates a fair agreement for the main features of cylindrical pores. The phenomenon of hysteresis has been also addressed in Ref. [8], it was found a good correspondence with results reported in the pioneering work of Cole and Saam [10].

Currently there is an increasing interest for investigating the storage capacity of small pores with different geometries (e.g., nanotubes and rather spherical zeo-

lites, see Ref. [7] and references quoted therein). According to this trend, the study of adsorption in spherical nano-cavities becomes relevant. Therefore the aim of the present work is to analyze phase transitions for classical and quantum fluids of noble gases confined into alkali metal cavities. We selected these systems because the involved interactions are known. Its behavior has been obtained from the SFM outlined above. In order to check the validity of such a rather crude model for this geometry, the adsorption of ^4He is also calculated by applying a DF. The latter approach has been recently successfully utilized for investigating properties of ^4He adsorbed on very small spherical balls (with radii of a few Å) of different materials [11,12]. However, for the sake of completeness, we should mention that Monte Carlo [13–15] as well as DF [15,16] calculations have been performed for classical gases adsorbed on planar alkali metals.

The paper is organized in the following way. In Sec. II we describe the evaluation of the adsorption potential and outline both the SFM and the DF approaches for capillary condensation. The numerical results and an improvement of the bare SFM are presented in Sec. III together with a discussion of the hysteresis cycles and a summary of the whole picture exhibited by the systems. Section IV is devoted to final remarks.

II. THE MODEL

The properties of a fluid adsorbed by a solid substrate may be studied by analyzing the grand free energy

$$\Omega[N] = F[N] - \mu N, \quad (2.1)$$

where F is the Helmholtz free energy, μ the chemical potential, and N the number of particles of the adsorbate. Quantity $F[N]$ contains the energy due to the interaction between fluid atoms as well as the energy provided by the confining potential. Let us first outline our approach for the description of the fluid-substrate interaction.

A. Adsorption potential

In order to construct the physisorption potential inside a spherical cavity we assume that an adsorbed atom located at \vec{r} , measured from the pore center, interacts with an elementary substrate volume at \vec{r}' via an isotropic

(12,6) Lennard-Jones (LJ) pair potential with standard parameters ε_{LJ} and σ_{LJ} . Next, we suppose that substrate atoms are uniformly distributed over the volume outside the cavity, this continuous substrate approximation leads to a spherically averaged potential. Under these conditions, when the substrate extends from $r = R_p$ up to $r = \infty$, the total potential may be expressed as

$$U_{\text{sub}}(r) = 8\pi \varepsilon_{LJ} \rho_{\text{sub}} \int_{R_p}^{\infty} r t^2 dr / \times \int_0^{\pi} \left[\left(\frac{\sigma_{LJ}}{|\vec{r} - \vec{r}'|} \right)^{12} - \left(\frac{\sigma_{LJ}}{|\vec{r} - \vec{r}'|} \right)^6 \right] \sin \theta d\theta. \quad (2.2)$$

Here, ρ_{sub} is the averaged density of the substrate in number of atoms per unit volume. Of course, each approximation performed along this procedure introduces an error. However, we expect that the resulting potential would give a fair description of the main features of examined systems. Notice that this procedure has been previously adopted in Refs. [17,18] for getting the plain (9,3) potential in the case of planar surfaces.

After some straightforward algebra the integral over θ may be cast into the form

$$I(r, r') = \int_0^{\pi} \left[\left(\frac{\sigma_{LJ}}{|\vec{r} - \vec{r}'|} \right)^{12} - \left(\frac{\sigma_{LJ}}{|\vec{r} - \vec{r}'|} \right)^6 \right] \sin \theta d\theta = \left(\frac{\sigma_{LJ}}{r'} \right)^{12} M_6(\nu) - \left(\frac{\sigma_{LJ}}{r'} \right)^6 M_3(\nu), \quad (2.3)$$

where $M_n(\nu)$ stands for the integral

$$M_n(\nu) = \int_0^{\pi} \frac{\sin \theta d\theta}{(1 + \nu^2 - 2\nu \cos \theta)^n} = \int_{-1}^1 \frac{dx}{(1 + \nu^2 + 2\nu x)^n} = \frac{1}{2(n-1)\nu} \left[\frac{1}{(1-\nu)^{2(n-1)}} - \frac{1}{(1+\nu)^{2(n-1)}} \right], \quad (2.4)$$

with $\nu = r/r'$. The integration over r' yields the following expression for the adsorption potential

$$U_{\text{sub}}(r) = \frac{16\pi}{3} \varepsilon_{LJ} \rho_{\text{sub}} R_p^3 \times \left[\frac{(15r^6 + 63r^4 R_p^2 + 45r^2 R_p^4 + 5R_p^6) \sigma_{LJ}^{12}}{15(R_p - r)^9 (R_p + r)^9} - \frac{\sigma_{LJ}^6}{(R_p - r)^3 (R_p + r)^3} \right]. \quad (2.5)$$

This formula may be compared with expressions derived in Ref. [19]. On the other hand, in the limit of a very large cavity ($R_p \rightarrow \infty$) an expansion in terms of $z = R_p - r \ll R_p$ reduces Eq. (2.5) to the (9-3) potential corresponding to a planar substrate (cf. Eq. (4) in [18])

$$U_{\text{sub}}(z) = \frac{4\pi}{3} \varepsilon_{LJ} \sigma_{LJ}^3 \rho_{\text{sub}} \left[\frac{1}{15} \left(\frac{\sigma_{LJ}}{z} \right)^9 - \frac{1}{2} \left(\frac{\sigma_{LJ}}{z} \right)^3 \right]. \quad (2.6)$$

For all the inert gases, the substrate potentials produced by pores in different alkali metals were calculated using values of ε_{LJ} and σ_{LJ} determined by adjusting the pair potentials of Patil [20] according to a procedure outlined by Ancilotto *et al.* [21]. Density ρ_{sub} was evaluated by taking into account that solid alkali metals are bcc crystals with a lattice constants a listed in Table 3 of [22]. All the adopted parameters are quoted in Tables I and II.

B. Simple fluid model

An expression for the Helmholtz free energy per particle for the CC phase, f_{CC} , may be obtained from the formalism developed in [5,6]. Assuming that the free energy of the fluid is given by the main contributions of the volume, surface, and substrate terms; then, if the fluid fills a pore forming a sharp sphere of radius R_0 with density equal to the bulk equilibrium value ρ_0 one gets

$$f_{\text{CC}} = \frac{F_{\text{CC}}}{N} = f_{\infty} + \sigma_{lv} \left(\frac{36\pi}{\rho_0^2} \right)^{1/3} N^{-1/3} + 4\pi \rho_0 \left\{ \int_0^{R_0} r^2 dr U_{\text{sub}}(r) \right\} N^{-1}, \quad (2.7)$$

with

$$N = 4\pi \int_0^{R_0} r^2 dr \rho(r) = \frac{4\pi}{3} \rho_0 R_0^3. \quad (2.8)$$

Here f_{∞} is the asymptotic value and it coincides with the chemical potential μ_0 at saturated vapor pressure (SVP). This expression for the free energy has been recently utilized for studying adsorption into cylindrical pores [6,8].

In all the cases, for a spherical cavity with a certain radius R_p the potential $U_{\text{sub}}(r)$ given by Eq. (2.5) exhibits a minimum with depth D_{R_p} at a distance $r_m(R_p)$ from the wall. It can be analytically shown that for a given fluid-substrate combination, in the regime $R_p > \sigma_{LJ}$, the depth D_{R_p} decreases for increasing size of the spherical cavity and attains an asymptotic value D_{∞} according to the expression

$$D_{R_p} = D_{\infty} \left[1 + \frac{27R^*}{4(2R^* - 1)^2} - \frac{3}{8(2R^* - 1)^3} - \frac{5 - 54R^* + 216R^{*2} - 504R^{*3} + 576R^{*4} - 288R^{*5}}{8(2R^* - 1)^9} \right], \quad (2.9)$$

where

$$D_{\infty} = \frac{2\sqrt{10}}{9} \pi \rho_{\text{sub}} \varepsilon_{LJ} \sigma_{LJ}^3, \quad (2.10)$$

and being the dimensionless pore radius

$$R^* = R_p/r_m. \quad (2.11)$$

Here r_m is the asymptotic position of the minimum [$r_m(R_p \rightarrow \infty)$] which is given by

$$r_m = \left(\frac{2}{5}\right)^{1/6} \sigma_{LJ}. \quad (2.12)$$

The behavior of D_{R_p}/D_∞ as a function of $1/(R^* - 1/2)$ is similar to that previously obtained for the cylindrical geometry (see Figs. 1 and 2 in [8] and Fig. 1 in [30]). In order to facilitate any comparison the values of r_m and D_∞ are listed in Table II. Since the properties found for the adsorption into cavities in Rb and K do not differ much from those for pores in Cs, the corresponding values are not included in this table. Note that for a given fluid-substrate system, the present r_m is larger than the corresponding parameter for a slit geometry z_m determined from a (9,3) potential in Ref. [3] (cf. Table I therein). This feature is simply due to different approaches used to fix the potential parameters.

1. Capillary condensed droplet phase

Upon taking into account Eqs. (2.7) and (2.8), and defining the sharp sphere radius R_0 as the effective pore radius $R_0 = R_p - r_m$, the grand thermodynamic potential for the CC phase becomes

$$\begin{aligned} \Omega_{CC} &= F_{CC} - \mu N \\ &= 4\pi\sigma_{lv}(R_p - r_m)^2 + 4\pi\rho_0 \int_0^{R_p - r_m} r^2 dr U_{sub}(r) \\ &\quad - \frac{4\pi}{3}(\mu - \mu_0)\rho_0(R_p - r_m)^3. \end{aligned} \quad (2.13)$$

Starting from this equation, it is possible to get the modified Kelvin equation (KE) for CC. By setting $\Omega_{CC} = 0$, one arrives at

$$\sigma_{sl} - \frac{1}{3}(\mu - \mu_0)\rho_0(R_p - r_m) = 0, \quad (2.14)$$

where σ_{sl} is the liquid-substrate interfacial tension defined as the sum

$$\begin{aligned} \sigma_{sl} &= \sigma_{lv} + \frac{\rho_0}{(R_p - r_m)^2} \int_0^{R_p - r_m} r^2 dr U_{sub}(r) \\ &= \sigma_{lv} + I_U, \end{aligned} \quad (2.15)$$

Next, by using the Gibbs-Duhem [31] relation for the fluid and neglecting any compression of the system one gets a link to the pressure P

$$\rho_0(\mu - \mu_0) = P - P_0, \quad (2.16)$$

which leads to the usual KE

$$3\sigma_{sl} - (P - P_0)(R_p - r_m) = 0. \quad (2.17)$$

This equation expresses the pressure reduction for condensation in terms of the effective radius of the condensed

fluid ($R_p - r_m$). The purpose of this work is to generalize the KE by taking into account both: (i) the explicit dependence of Ω_{CC} on the substrate potential and (ii) the role of film formation on the adsorption behavior.

For the sake of generality, we shall discuss the predictions in terms of the dimensionless grand potential

$$\Omega^* = \frac{\Omega}{A\sigma_{lv}}, \quad (2.18)$$

which for the CC phase may be written as

$$\begin{aligned} \Omega_{CC}^* &= \frac{\Omega_{CC}}{A\sigma_{lv}} = \frac{F_{CC} - \mu N}{4\pi(R_p - r_m)^2\sigma_{lv}} \\ &= 1 + \frac{I_U}{\sigma_{lv}} - \frac{1}{3} \frac{(\mu - \mu_0)\rho_0}{\sigma_{lv}} (R_p - r_m). \end{aligned} \quad (2.19)$$

It is convenient to cast the integrated adsorption potential per unit area I_U in the following reduced form

$$\begin{aligned} I_U^* &= \frac{I_U}{\sigma_{lv}} \\ &= -\frac{D_\infty\rho_0}{\sigma_{lv}(R_p - r_m)^2} \int_0^{R_p - r_m} r^2 dr [-U_{sub}(r)/D_\infty] \\ &= -\frac{1}{2}D^*g\{R^* - 1\}, \end{aligned} \quad (2.20)$$

Here, the strength parameter is the reduced asymptotic well depth

$$D^* = 2 \frac{D_\infty r_m \rho_0}{\sigma_{lv}} = \frac{4(20)^{1/3}\pi}{9} \rho_{sub} \varepsilon_{LJ} \sigma_{LJ}^4 \frac{\rho_0}{\sigma_{lv}}. \quad (2.21)$$

and $g\{R^* - 1\}$ is the dimensionless integral

$$g\{\xi\} = \frac{1}{\xi^2} \int_0^\xi \xi'^2 d\xi' [-U_{sub}(r_m \xi')/D_\infty], \quad (2.22)$$

with

$$\xi = r/r_m. \quad (2.23)$$

Consequently, one has also to introduce the reduced difference of chemical potentials

$$\Delta = (\mu_0 - \mu)r_m\rho_0/\sigma_{lv}. \quad (2.24)$$

These definitions of D^* and Δ are formally equal to those adopted in previous works [3,8], provided that for planar parallel walls instead of r_m one uses z_m .

Finally, one may write the reduced version of the grand potential given by Eq. (2.19) in the following way

$$\Omega_{CC}^* = 1 - \frac{1}{2}D^*g\{R^* - 1\} + \frac{1}{3}\Delta(R^* - 1). \quad (2.25)$$

This expression allows a study of adsorption in terms of D^* . Before going ahead, let us remind that a fundamental property of the integral $g\{\xi\}$ introduced by Eq. (4)

in [3] is its independence of the fluid-substrate combination. This feature is also exhibited by the integral $g\{\xi\}$ calculated according to Eq. (2.22)

$$g\{\xi\} = -\frac{2}{3} \frac{R^{*3} \xi (5 R^{*4} + 14 R^{*2} \xi^2 + 5 \xi^4)}{(R^{*2} - \xi^2)^8} + \frac{3}{2} \frac{R^* (R^{*2} + \xi^2)}{\xi (R^{*2} - \xi^2)^2} - \frac{3}{4} \frac{1}{\xi^2} \ln \left[\frac{R^* + \xi}{R^* - \xi} \right]. \quad (2.26)$$

For $\xi = R^* - 1$, in the limiting case $R^* \rightarrow \infty$ one gets

$$\lim_{R^* \rightarrow \infty} g\{R^* - 1\} = \frac{11}{16}. \quad (2.27)$$

This result is equal to that obtained for the slit geometry [3].

2. Shell-film phase

Under the same assumptions adopted for writing Eqs. (2.7) and (2.13), the grand thermodynamic potential for a spherical film of thickness ℓ , i.e., for the shell-film (SF) phase, may be expressed as

$$\begin{aligned} \Omega_{\text{SF}} &= F_{\text{SF}} - \mu N \\ &= 4\pi \sigma_{lv} [(R_p - r_m)^2 + (R_p - r_m - \ell)^2] \\ &\quad + 4\pi \rho_0 \int_{R_p - r_m - \ell}^{R_p - r_m} r^2 dr U_{\text{sub}}(r) \\ &\quad - \frac{4\pi}{3} (\mu - \mu_0) \rho_0 [(R_p - r_m)^3 - (R_p - r_m - \ell)^3]. \end{aligned} \quad (2.28)$$

Note that the film grows from $r = r_m$ towards the center. The reduced version of this grand free energy reads

$$\begin{aligned} \Omega_{\text{SF}}^* &= \frac{\Omega_{\text{SF}}}{4\pi R_0^2 \sigma_{lv}} = 1 + \left(1 - \frac{x}{R^* - 1}\right)^2 - \frac{1}{2} D^* \\ &\quad \times \left[g\{R^* - 1\} - \left(1 - \frac{x}{R^* - 1}\right)^2 g\{R^* - 1 - x\} \right] \\ &\quad + \frac{1}{3} \Delta (R^* - 1) \left[1 - \left(1 - \frac{x}{R^* - 1}\right)^3 \right], \end{aligned} \quad (2.29)$$

where x is the dimensionless thickness

$$x = \ell/r_m, \quad (2.30)$$

which is related with the dimensionless inner radius y measured from the center of the sphere

$$y = (R_p - r_m - \ell)/r_m = R^* - 1 - x. \quad (2.31)$$

In this case, in order to find the stable configuration at fixed R^* (i.e., $R_p = \text{const.}$), one must determine the value of x which provides the minimum Ω_{SF}^* .

C. Density functional theory

In the DF approach the ground-state energy of an interacting N -body system of ${}^4\text{He}$ atoms, confined by an adsorbate-substrate potential $U_{\text{sub}}(\mathbf{r})$, may be written as

$$\begin{aligned} E_{\text{gs}} &= -\frac{\hbar^2}{2m} \int d\mathbf{r} \sqrt{\rho(\mathbf{r})} \nabla^2 \sqrt{\rho(\mathbf{r})} + \int d\mathbf{r} \rho(\mathbf{r}) e_{\text{sc}}(\mathbf{r}) \\ &\quad + \int d\mathbf{r} \rho(\mathbf{r}) U_{\text{sub}}(\mathbf{r}), \end{aligned} \quad (2.32)$$

where $\rho(\mathbf{r})$ is the one-body density and $e_{\text{sc}}(\mathbf{r})$ the self-correlation energy per particle. The density profile $\rho(\mathbf{r})$ is determined from the Euler-Lagrange (EL) equation derived from the condition

$$\frac{\delta \Omega}{\delta \rho(\mathbf{r})} = \frac{\delta \{ E_{\text{gs}}[\rho, \nabla \rho] - \mu N \}}{\delta \rho(\mathbf{r})} = 0. \quad (2.33)$$

In the case of a spherical symmetry the variation of Eq. (2.33) leads to the following Hartree like equation for the square root of the one-body helium density

$$\begin{aligned} -\frac{\hbar^2}{2m} \left(\frac{d^2}{dr^2} + \frac{2}{r} \frac{d}{dr} \right) \sqrt{\rho(r)} \\ + \left[V_H(r) + U_{\text{sub}}(r) \right] \sqrt{\rho(r)} = \mu \sqrt{\rho(r)}, \end{aligned} \quad (2.34)$$

which also determines μ . Here $V_H(\mathbf{r})$ is a Hartree mean-field potential given by the first functional derivative of the total correlation energy $E_{\text{sc}}[\rho]$

$$V_H(\mathbf{r}) = \frac{\delta E_{\text{sc}}[\rho]}{\delta \rho(\mathbf{r})} = \frac{\delta}{\delta \rho(\mathbf{r})} \int d\mathbf{r}' \rho(\mathbf{r}') e_{\text{sc}}(\mathbf{r}'). \quad (2.35)$$

The expression for the spherically symmetric $V_H(r)$ derived in the case of the Orsay-Paris nonlocal DF (OP-NLDF) proposed in [32] is given in the Appendix of [33]. Equation (2.34) was solved at a fixed number of helium atoms

$$N = 4\pi \int_0^\infty r^2 dr \rho(r). \quad (2.36)$$

III. GENERAL RESULTS - PHASE DIAGRAMS

A. Thresholds for CC and SF phases at SVP

The case of SVP ($\Delta = 0$) leads to a very simple criterion for the occurrence of CC. The expression for the transition line ($\Omega_{\text{CC}}^* = 0$) which separates the behavior into two regimes, capillary condensation ($\Omega_{\text{CC}}^* < 0$) or empty ($\Omega_{\text{CC}}^* > 0$), is

$$D_{\Delta=0}^*(\text{CC}) = \frac{2}{g\{R^* - 1\}}. \quad (3.1)$$

It coincides with Eq. (7) of [3] and with Eq. (3.1) of [8]. Its dependence on R^* is displayed in Fig. 1. Therefore, one can state that the curve given by Eq. (3.1) provides a universal relation for the critical values of the parameters R^* and $D_{\Delta=0}^*$. On the other hand, it should be noticed that at SVP the transition from empty (E) to SF would occur for

$$D_{\Delta=0}^*(\text{SF}) = \frac{2(R^* - 1)^2 + 2(R^* - 1 - x)^2}{(R^* - 1)^2 g\{R^* - 1\} - (R^* - 1 - x)^2 g\{R^* - 1 - x\}}. \quad (3.2)$$

It is clear that, for $0 < x < R^* - 1$, $D_{\Delta=0}^*(\text{SF})$ is always larger than $D_{\Delta=0}^*(\text{CC})$. So, for increasing D^* at SVP, before Ω_{SF}^* becomes zero Ω_{CC}^* is already negative favoring the CC phase against the SF one.

Furthermore, the threshold condition for CC to occur at SVP for large R^* changes very little for increasing R^* and for very broad pores attains the asymptotic value

$$D_{\Delta=0}^*(\text{CC}; R^* \rightarrow \infty) = \lim_{R^* \rightarrow \infty} \left[\frac{2}{g\{R^* - 1\}} \right] = \frac{32}{11} \simeq 2.9. \quad (3.3)$$

A glance at Table II indicates that noble gases heavier than ${}^4\text{He}$ adsorbed in cavities of Cs would not form in the present approach a stable CC phase at the triple-point temperature $T = T_t$, because the corresponding values of D^* are smaller than 2.9.

B. Thresholds for CC and SF phases below SVP

The general problem of behavior below SVP is more complicated. The presence of the Δ term in Eq. (2.25) leads to the following threshold value for CC

$$D^*(\text{CC}) = D_{\Delta=0}^*(\text{CC}) \left[1 + \frac{1}{3} \Delta (R^* - 1) \right]. \quad (3.4)$$

However, one must now examine the possibility that a film configuration has a lower free energy than that of the CC phase. So, in the case $\Delta > 0$, it is necessary to evaluate the minimum of Ω_{SF}^* as a function of the variable x and to compare the result with Ω_{CC}^* .

The reduced depth for $\text{E} \rightarrow \text{SF}$ transition at $\Delta > 0$ may be obtained from Eq. (2.29), written in terms of y it becomes

$$D^*(\text{SF}) = D_{\Delta=0}^*(\text{SF}) \left[1 + \frac{1}{3} \Delta \frac{(R^* - 1)^3 - y^3}{(R^* - 1)^2 + y^2} \right]. \quad (3.5)$$

The difference between the grand free energy of the SF phase and that of the CC case written in terms of the dimensionless inner radius y is

$$\Omega_{\text{SF}}^* - \Omega_{\text{CC}}^* = \left(\frac{y}{R^* - 1} \right)^2 \left(1 + \frac{1}{2} D^* g\{y\} - \frac{1}{3} \Delta y \right). \quad (3.6)$$

Here, in the second parenthesis, the first term represents the extra surface energy of the film, the second provides the interaction between the solid substrate and the adsorbed atoms which fill the gap when the SF to CC transition occurs; while the third stands for the free energy cost because the system is (in general) below SVP. When the internal radius of the shell film goes to zero, i.e. $y \rightarrow 0$, the difference of grand potentials given by Eq. (3.6) vanishes. The threshold value for the transition SF \rightarrow CC is

$$D^*(\text{SF} \rightarrow \text{CC}) = \frac{2}{g\{y\}} \left[-1 + \frac{1}{3} \Delta y \right], \quad (3.7)$$

provided that y is taken at the minimum of Ω_{SF}^* .

Before describing the general phase diagram of the systems for any $\Delta > 0$, it is useful to examine with some detail data calculated for a fixed value of Δ . Figure 2 shows results obtained for $\Delta = 0.2$ by varying D^* and R^* . In this case some features of Ω_{CC}^* and Ω_{SF}^* are explicitly indicated. Solid lines separate domains of stable phases. Note that there is a “triple point” below which the space is empty (E), to the upper right of which there is a SF region, and to the upper left there is CC. The dashed straight line in the SF region is the threshold given by Eq. (3.4), while dashed curves in the CC regime denote the limit for SF solutions determined by the threshold given by Eq. (3.5) and the disappearance of the minimum of Ω_{SF}^* . So, the hatched zones indicate parameter regions where both CC and SF are negative. However, only that phase with lower Ω^* is stable, the other one is metastable and plays an important role in the cycle of hysteresis to be addressed later in the paper.

Let us now turn to the general phase diagram. The results for several values of Δ are displayed in Fig. 1, where only boundaries between stable phases are indicated. Increasing D^* favors SF or CC phases against the E phase. Which of the condensed phases is stable depends on R^* . For large R^* , SF is typically favored because of the cost of CC (the Δ term) becomes large relative to the benefits (from the potential and the decrease of surface energy). The SF to E transition curve is rather insensitive to R^* .

Figures 3 and 4 show the reduced phase diagrams projected onto the $R^* - \Delta$ plane for $D^* = 5.84$ and 11.87 (i.e. for the ${}^4\text{He}/\text{Cs}$ and ${}^4\text{He}/\text{Na}$ cases, respectively). However, for other values of D^* the shape of the corresponding curves is similar. The curves indicate the transitions between stable phases. These plots also include threshold values obtained from OP-NLDF calculations for $R_p = 10, 12, 15, 20$, and 30 \AA . For ${}^4\text{He}/\text{Na}$ these results lie in the neighbor of the “triple point” determined by the joining of all three E, SF, and CC phases, where the solutions are sensitive to changes of Δ . Note that the E \rightarrow CC and SF \rightarrow CC transitions provided by the SFM

occur at almost the same values of Δ as that determined from OP-NLDF. There is no SF phase for $^4\text{He}/\text{Cs}$ systems in the analyzed range of R^* . On the other hand, the predictions for the E \rightarrow SF transition do not match so well. All these features of the agreement are similar to that previously found for planar and cylindrical systems (see Fig. 4 in [3] and Fig. 6 in [8]).

C. Correction to the bare simple fluid model

The prediction given by the bare SFM for the E \rightarrow SF phase transition may be improved by introducing a correction to the surface term in Ω_{SF} . By looking at the surface energy term in Eq. (2.28), which is proportional to σ_{lv} , one realizes that it does not vanish in the limit of a zero-thickness film (i.e. for $\ell \rightarrow 0$). In order to eliminate this shortcoming one may follow an idea adopted by Cheng *et al.* [34] in writing their Eq. (2.4). Accordingly, we shall assume that the surface contribution grows exponentially from zero at $\ell = 0$ to the bare value $4\pi\sigma_{lv}[(R_p - r_m)^2 + (R_p - r_m - \ell)^2]$ over a characteristic length ζ

$$\Omega_{\text{SF}}(\text{surf}) = 4\pi\sigma_{lv}[(R_p - r_m)^2 + (R_p - r_m - \ell)^2] \times \left[1 - \exp(-\ell/\zeta)\right]. \quad (3.8)$$

This leads to the reduced version

$$\Omega_{\text{SF}}^*(\text{surf}) = \left[1 + \left(1 - \frac{x}{R^* - 1}\right)^2\right] \left[1 - \exp(-\beta x)\right], \quad (3.9)$$

with

$$\beta = r_m/\zeta. \quad (3.10)$$

Let us now analyze the changes of the energetics due to this cut-off factor. As expected, its effect only becomes important for rather thin films. In the frame of the improved SFM the E \rightarrow SF transition is reached for a larger value of $\mu_0 - \mu$ than in the original version. Both these features can be observed in Fig. 5, where results for ^4He adsorbed into a spherical Na cavity with radius $R_p = 30 \text{ \AA}$ are shown. Hence, the more elaborated approach yields a better agreement with OP-NLDF results. In fact, for the $^4\text{He}/\text{Na}$ systems a very good agreement is obtained with $\beta_a = 3.3$ as shown in Fig. 4. It should be noted that the corrected curves for the E \rightarrow CC and SF \rightarrow CC transitions cannot be distinguished from the previous ones on the scale of the drawing.

It is plausible to assume that the characteristic length ζ be mainly proportional to the asymptotic width W_∞ of a free ^4He surface. So, one may write

$$\beta = r_m/\zeta = \lambda r_m/W_\infty = \lambda/W^*, \quad (3.11)$$

where W^* is the dimensionless asymptotic width

$$W^* = W_\infty/r_m. \quad (3.12)$$

By using the asymptotic value $W_\infty \simeq 6 \text{ \AA}$ [33], for $^4\text{He}/\text{Na}$ systems one gets $W^* \simeq 1.3$, which leads to $\lambda_a \simeq 4.3$. A critical film thickness ℓ_a may be defined by requiring that the exponential of Eq. (3.8) be reduced from unity to about 0.1, i.e. so that the surface energy reach a 90% of its bare value of Eq. (2.28). This choice for the decay coincides with the density fall off adopted for defining the surface thickness in the literature [33]. Following this procedure, the obtained value of λ_a yields $x_a/W^* = \ell_a/W_\infty \simeq 0.54$. This means that, in the improved SFM the bare value of the surface energy will be essentially reached when an adsorbed film of uniform density ρ_0 would have approximately the number of helium atoms enough to develop a surface with thickness W_∞ at its internal face.

In Figs. 6 and 7 we compare the chemical potentials, the free energies and grand free energies per particle provided by the improved SFM with results obtained from the OP-NLDF calculations. The data correspond to ^4He adsorbed into cavities of Cs and Na with radius $R_p = 30 \text{ \AA}$. These plots show a good qualitative agreement between both theoretical approaches, of coarse, there are some quantitative differences. Note that in the case of $^4\text{He}/\text{Na}$ a Maxwell construction is required in order to determine $\mu_0 - \mu = 3.7 \text{ K}$ from OP-NLDF data for the SF \rightarrow CC transition.

An example of the density profile evolution as a function of the number of ^4He atoms is shown in Fig. 8. There OP-NLDF results, including the metastable (or unstable) solutions, obtained for a Na cavity with radius $R_p = 30 \text{ \AA}$ are displayed. One may observe that the growth of the density profile is continuous and relatively smooth throughout the available space.

It is worthy of notice that the value $\beta_a = 3.3$ fixed above lies just in the parameter region determined by Cheng *et al.* [34] for approaching results given by the full NLDF theory in the case of planar geometry. Moreover, this β_a is close to $\beta = 3$ chosen in that paper for the purpose of illustration. Therefore it becomes of interest to make a connection to the paper of Calbi *et al.* [4] on ^4He confined by two parallel walls separated by a distance L . By looking at Figs. 15 and 16 of that work one may realize that predictions for the E \rightarrow F (film) phase transitions provided by the bare SFM do not reproduce quite well results given by the NLDF theory. So, we examined the extend to which a correction similar to that included in Eq. (3.8) can improve the agreement in the case of adsorption into slits. For such a geometry, the surface contribution to the reduced grand free energy is given by the factor 4 in Eq. (8) of Ref. [3]. Consequently, that term was rewritten as

$$\Omega_F^*(\text{surf}) = 4 \left[1 - \exp\left(-\frac{\lambda x}{W^*}\right)\right], \quad (3.13)$$

here W^* is

$$W^* = W_\infty/z_m. \quad (3.14)$$

All the reduced dimensionless quantities needed to treat a planar system can be obtained from Eqs. (1)-(6) in [4]. To illustrate the effect of this cut-off factor we selected the case of ^4He adsorbed between planar walls of Li. The evaluation was performed with the same cut-off parameter $\lambda_a \simeq 4.3$ utilized for spherical cavities. Figure 9 shows data reported in Fig. 15 of [4] together with the shift of the $\text{E} \rightarrow \text{F}$ transition towards larger Δ . From this plot one may conclude, that also for the planar geometry the agreement with NLDF results is significantly improved. As before the $\text{E} \rightarrow \text{CC}$ and $\text{SF} \rightarrow \text{CC}$ transitions remain almost unchanged.

D. Critical radii and adsorption process

Let us now refer to the phenomenon of hysteresis inherently related to capillary condensation. For the analysis to be made in this section it is convenient to define a reduced inner radius η as

$$\eta = \frac{y}{R^* - 1} = 1 - \frac{x}{R^* - 1}. \quad (3.15)$$

Since the empty fraction of the cavity is η^3 , for $\eta = 0$ capillary condensation with a completely filled pore occurs, while in the $\eta \rightarrow 1$ limit for large R^* there are very narrow shell films adsorbed on the substrate wall. We determined two families of critical inner radii: η_M at which the solution for SF becomes metastable and η_C at which SF becomes unstable. Associated to the critical radii η_M and η_C there are critical reduced chemical potentials Δ_M and Δ_C . Numerous experimental evidences reported in the literature indicate that porous materials fill and drain at different values of the chemical potential leading to loops of hysteresis (see Lilly and Hallock [35] and references quoted therein). In order to explain these loops it was suggested by Cole and Saam [10] that the process of adsorption and desorption of a single cavity do not always follow the path guided by stable phases. The idea is that physical systems exhibit a sort of memory trying to remain in the initial phase when Δ is changed.

The filling and draining of a spherical cavity may be followed by looking at Fig. 6 of Ref. [35]. This process can be analyzed by examining Figs. 4 and 10. For a fixed pore size and a given adsorbate-substrate combination, the adsorption starts at $\Delta > 0$ in an E phase, which corresponds to the vapor phase of the fluid. Next, the filling of the pore by decreasing Δ increases the vapor density (this behavior is not included in the SFM, in which all the gas states are considered E phase). At some value of Δ the SF phase becomes stable and a thin shell film is formed, then it grows increasing its thickness x and reducing the inner radius η up to the crossing of Ω_{SF}^* with Ω_{CC}^* . The key assumption for building an elementary

hysteretic loop [10] is that after this crossing the filling follows the metastable SF phase up to the critical point (Δ_C, x_C) where it becomes unstable. Then the $\text{SF} \rightarrow \text{CC}$ transition must occur as indicated in Fig. 8(b) of [8]. By draining the transition $\text{CC} \rightarrow \text{SF}$ occurs at (Δ_M, η_M) giving rise to an elementary loop of hysteresis. If R^* is sufficiently small the SF phase cannot exist and the filling jumps directly from E to CC following a simpler path and no hysteresis takes place. In fact, the whole process described here is equal to that assumed in the case of cylindrical pores [8,10,35].

Figure 10 shows results obtained for adsorption of noble gases into cavities of Na and Li, for these adsorbate-substrate systems D^* is always larger than 2.9. For each system the *nearly* universal behavior starts at about $R^* - 1 \simeq 15$, which for D^* in the range 4 → 20 yields for the abscissa

$$\Psi = \frac{R^* - 1}{\sqrt{D^*}} \quad (3.16)$$

values between 7.5 and 3.6. The limiting curves for metastable and unstable SF solutions may be derived from expansions in powers of $1/\sqrt{D^*}$. Upon keeping the leading term only, the explicit formula for the metastable border reads

$$\Psi_M^2 = \frac{3}{8} \left[\frac{6\eta^4 + 16\eta^2 - 6}{\eta(1-\eta^2)^3} + \frac{3}{\eta^2} \ln \left(\frac{1+\eta}{1-\eta} \right) \right], \quad (3.17)$$

while for the unstable one becomes

$$\Psi_C^2 = \frac{18\eta^3}{(1-\eta^2)^4}. \quad (3.18)$$

These functions are also plotted in Fig. 10, where one may observe that its behavior is similar to that found before for cylindrical pores in terms of hypergeometric functions (see Fig. 10 in [8] and Fig. 2 in [10]). The limiting curve corresponding to $\text{E} \rightarrow \text{SF}$ lies at $\eta = 1$.

IV. FINAL REMARKS

A SFM is used for studying adsorption into isolated spherical cavities. This model has previously been successfully applied for analyzing phase transitions in the cases of planar slits [3] and cylindrical pores [8]. For the spherical geometry treated in the present work the SFM yields a *universal* description of capillary condensation transitions for noble gases confined in pores of alkali metals providing an interpretation of the wide range of behavior which can occur. This *universality* is due to the fact that the integrated adsorption potential $g\{\xi\}$ expressed in dimensionless quantities [see Eqs. (2.22) and (2.26)] is a *universal* function of $\xi = r/r_{\min}$. This property is a consequence of the continuous substrate approximation. Planar slits and cylindrical pores also exhibit this feature, but in the last geometry to get $g\{\xi\}$ one must perform numerical integrations [8].

The phase diagram for spherical cavities displayed in Fig. 1 is qualitatively equivalent to that previously obtained in for planar and cylindrical geometries (see Fig. 2 in [3] and Fig. 3 in [8]).

The reliability of the SFM was checked by performing a comparison with results provided by the much more realistic OP-NLDF. In the latter case the calculations were carried out for increasing number of ^4He atoms within spherical cavities of different radii. It was found that for the $\text{E} \rightarrow \text{CC}$ and $\text{SF} \rightarrow \text{CC}$ phase transitions there is a rather good agreement between both approaches (see Figs. 3 and 4), while for the $\text{E} \rightarrow \text{SF}$ one there is a sizeable difference as indicated by Fig. 4.

It is shown that the bare SFM for shell films given by Eq. (2.28) may be improved by including a correction to the surface contribution. As can be seen in Figs. 4, 5, and 7, the effect of this improvement becomes important for thin films. These plots show that the transitions between stable phases occur at virtually the same value of Δ in the OP-NLDF theory and in the improved SFM. Furthermore, the application of the latter approach for planar slits also yields better agreement with NLDF results as shown in Fig. 9.

According to our calculations almost all the examined adsorbate-substrate combinations will form CC at $T = T_t$, the exceptions are Ne, Ar, Kr, and Xe adsorbed into cavities of Cs. In these cases it becomes necessary an extra determination of critical temperatures for CC like it has been done in [8]. In this respect, it should be mentioned that it has been previously found that neither Ne confined by planar walls of Cs [3] nor Ne and Ar adsorbed into cylinders of Cs [8] form CC at $T = T_t$, showing a systematic dependence on the pore curvature.

The critical radii for metastable phases and unstable films displayed in Fig. 10 resemble the behavior found previously for cylindrical pores [8,10]. So, adsorption potentials built up for different curved geometries lead to qualitatively similar features. On the other hand, it is suggested how an elementary hysteretic cycle could be constructed by filling and draining the cavity along paths determined by the critical points (Δ_M, η_M) and (Δ_C, η_C) .

In summary, we can state that the present work close successfully the application of the so called SFM for studying CC in pores exhibiting standard regular geometries, i.e. planar slits, cylindrical pores and spherical cavities.

ACKNOWLEDGMENTS

We thank Dr. E.S. Hernández for fruitful discussions. This work was supported in part by the Ministry of Culture and Education of Argentina through Grants AN-PCyT No. PICT2000-03-08540 and UBACYT No. EX-01/X103.

⁺ Also at the Comisión de Investigaciones Científicas de la Prov. de Buenos Aires, Calle 526 entre 10 y 11, RA-1900 La Plata, Argentina.

^{*} Also at the Carrera del Investigador Científico of the Consejo Nacional de Investigaciones Científicas y Técnicas, Av. Rivadavia 1917, RA-1033 Buenos Aires, Argentina.

- [1] E. Cheng, M. W. Cole, W. F. Saam, and J. Treiner, *Phys. Rev. B* **48**, 18214 (1993).
- [2] A. Chizmeshya, M. W. Cole, and E. Zaremba, *J. Low Temp. Phys.* **110**, 677 (1998).
- [3] S. M. Gatica, M. M. Calbi, and M. W. Cole, *Phys. Rev. E* **59**, 4484 (1999).
- [4] M. M. Calbi, F. Toigo, S. M. Gatica, and M. W. Cole, *Phys. Rev. B* **60**, 14935 (1999).
- [5] L. Szybisz, *Physica A* **283**, 193 (2000).
- [6] L. Szybisz and S. M. Gatica, *Phys. Rev. B* **64**, 224523 (2001).
- [7] S. M. Gatica, M. M. Calbi, M. W. Cole, *Phys. Rev. E* **65**, 061605 (2002).
- [8] L. Szybisz and I. Urrutia, *Phys. Rev. E* **66**, 051201 (2002).
- [9] I. Urrutia and L. Szybisz, *Physica A*, in press (2004).
- [10] M. W. Cole and W. F. Saam, *Phys. Rev. Lett.* **32**, 985 (1974).
- [11] E. S. Hernández, M. W. Cole, and M. Boninsegni, *Phys. Rev. B* **68**, 125418 (2003).
- [12] L. Szybisz and I. Urrutia, *J. Low Temp. Phys.* **134**, 1079 (2004).
- [13] M. J. Bojan, G. Stan, S. Curtarolo, W. A. Steele, and M. W. Cole, *Phys. Rev. E* **59**, 864 (1999).
- [14] S. Curtarolo, G. Stan, M. J. Bojan, M. W. Cole, and W. A. Steele, *Phys. Rev. E* **61**, 1670 (2000).
- [15] F. Ancilotto, S. Curtarolo, F. Toigo, and M. W. Cole, *Phys. Rev. Lett.* **87**, 206103 (2001).
- [16] F. Ancilotto and F. Toigo, *Phys. Rev. B* **60**, 9019 (1999).
- [17] T. L. Hill, *Adv. Catalysis* **4**, 211 (1952).
- [18] F. Ricca, *Nuovo Cim. Suppl.* **V**, 339 (1967).
- [19] I. Derycke, J. P. Vigneron, Ph. Lambin, A. A. Lucas, and E. G. Derouane, *J. Chem. Phys.* **94**, 4620 (1991).
- [20] S. H. Patil, *J. Chem. Phys.* **94**, 8089 (1991).
- [21] F. Ancilotto, E. Cheng, M. W. Cole, and F. Toigo, *Z. Phys. B: Condens. Matter* **98**, 323 (1995).
- [22] C. Kittel, *Introduction to Solid State Physics* (Wiley, New York, 1986), Chap. 1.
- [23] S. Stringari and J. Treiner, *Phys. Rev. B* **36**, 8369 (1987).
- [24] H. M. Guo, D. O. Edwards, R. E. Sarwinski, and J. T. Tough, *Phys. Rev. Lett.* **27**, 1259 (1971).
- [25] D. O. Edwards and W. F. Saam, in *Progress in Low Temperature Physics*, edited by D. F. Brewer (North-Holland, Amsterdam, 1978) Vol. 7A, Chap. 4.
- [26] M. Iino, M. Suzuki, and A. J. Ikushima, *J. Low Temp. Phys.* **61**, 155 (1985).
- [27] P. Roche, G. Deville, N. J. Appleyard, and F. I. B. Williams, *J. Low Temp. Phys.* **106**, 565 (1997).
- [28] S.-T. Wu and G.-S. Yan, *J. Chem. Phys.* **77**, 5799 (1982).

[29] L. W. Bruch, M. W. Cole, and E. Zaremba, *Physical Adsorption* (Oxford Univ. Press, Oxford, 1997).

[30] G. Stan and M. W. Cole, *Surf. Sci.* **395**, 280 (1998).

[31] J. S. Rowlinson and B. Widom, *Molecular Theory of Capillarity* (Clarendon Press, Oxford, 1982).

[32] J. Dupont-Roc, M. Himbert, N. Pavloff, and J. Treiner, *J. Low Temp. Phys.* **81**, 31 (1990).

[33] L. Szybisz and I. Urrutia, *Phys. Rev. B* **68**, 054518 (2003).

[34] E. Cheng, M. W. Cole, W. F. Saam, and J. Treiner, *Phys. Rev. B* **46**, 13967 (1992).

[35] M. P. Lilly and R. B. Hallock, *Phys. Rev. B* **63**, 174503 (2001).

TABLE I. Experimental values of relevant observables for the inert gases in the liquid phase at the triple point and the lattice parameters of solid alkali metals.

System	T_t [K]	μ_0 [K]	ρ_0 [\AA^{-3}]	σ_{lv} [K/ \AA^2]	Ref.
^4He	0. ^a	-7.15	0.02184		[23]
				0.274 \pm 0.003	[24,25]
				0.257 \pm 0.001	[26]
				0.272 \pm 0.002	[27]
Ne	24.55	-232.	0.03694	3.98	[1,28,29]
Ar	83.81	-930.	0.02117	9.74	[1,28,29]
Kr	115.76	-1342.	0.01785	11.22	[1,28,29]
Xe	161.39	-1907.	0.01411	12.65	[1,28,29]
a [\AA] ^b ρ_{sub} [\AA^{-3}] ^c Ref.					
Cs	6.045	0.009054			[22]
Rb	5.585	0.0115			[22]
K	5.225	0.0140			[22]
Na	4.225	0.02652			[22]
Li	3.491	0.04701			[22]

^a The data for ^4He correspond to $T = 0$ K.

^b From Ref. [22].

^c Body centered cubic crystal structure.

TABLE II. Values of the LJ parameters for the interaction between noble gases and alkali metals, together with the asymptotic well depth and the location of the minimum corresponding to potentials given by Eq. (2.5).

System	ε_{LJ} [K] ^a	σ_{LJ} [\AA] ^a	r_m [\AA]	D_∞ [K]	D^*
He-Cs	1.21	6.47	5.55	6.55	5.84
He-Na	1.73	5.40	4.63	15.95	11.87
He-Li	1.92	5.22	4.48	28.34	20.39
Ne-Cs	8.65	5.23	4.49	24.73	2.06
Ne-Na	11.94	4.37	3.75	58.34	4.06
Ne-Li	13.33	4.23	3.63	104.7	7.06
Ar-Cs	51.79	4.86	4.17	118.8	2.15
Ar-Na	60.32	4.20	3.60	261.6	4.10
Ar-Li	66.00	4.08	3.50	465.2	7.08
Kr-Cs	87.16	4.75	4.08	186.7	2.42
Kr-Na	94.10	4.16	3.57	396.6	4.51
Kr-Li	100.10	4.06	3.48	695.2	7.71
Xe-Cs	117.2	4.87	4.18	270.6	2.52
Xe-Na	126.0	4.27	3.66	574.3	4.70
Xe-Li	135.8	4.16	3.57	1015	8.08

^a Parameters calculated with data taken from [20] by applying the procedure outlined in [21].

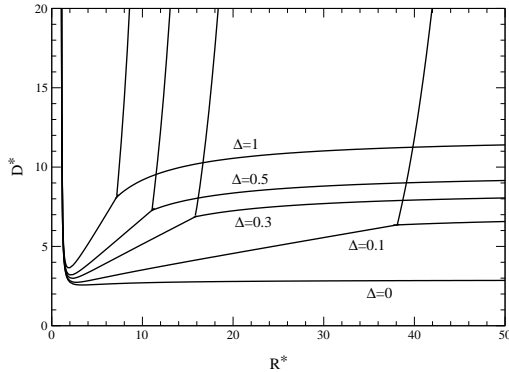


FIG. 1. Phase diagram showing the behavior at various degrees of undersaturation, expressed in terms of the reduced chemical potential difference Δ given by Eq. (2.24). For the case $\Delta = 0$, the line satisfies Eq. (3.1); all values above the curve correspond to capillary condensation, while those below are “empty”. For the other cases, $\Delta > 0$, there is a “triple point” below which the space is empty, to the upper right of which there is a shell film, and to the upper left there is capillary condensation.

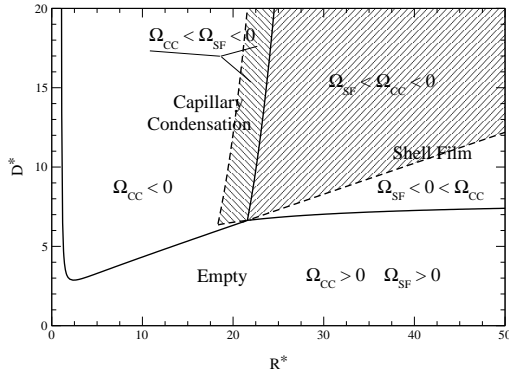


FIG. 2. Universal “phase diagram” showing regimes of empty, capillary condensed, and adsorbed shell film as a function of reduced pore radius and well depth defined in the text [see Eqs. (2.11) and (2.21)]. The displayed curves correspond to $\Delta = 0.2$. The hatched zones are regions where both Ω_{SF}^* and Ω_{CC}^* are negative.

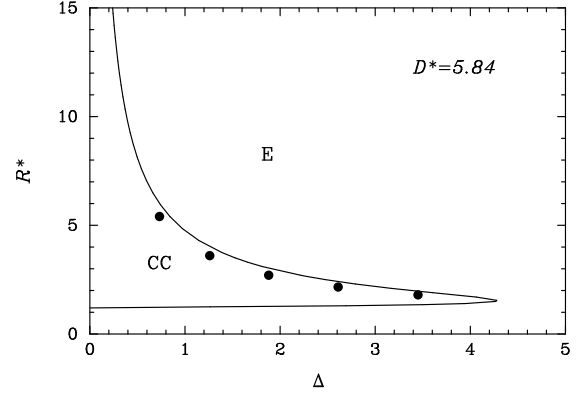


FIG. 3. Reduced phase diagram for $D^* = 5.84$ (i.e. ${}^4\text{He}/\text{Cs}$ in our approach). The curve indicates the prediction of the SFM for the boundary between possible stable phases (empty and capillary condensation). The full circles stand for transitions determined from OP-NLDF calculations.

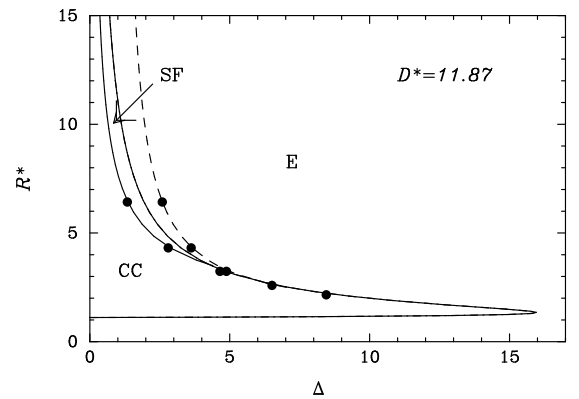


FIG. 4. Reduced phase diagram for $D^* = 11.87$ (i.e. ${}^4\text{He}/\text{Na}$ in our approach). The solid curves indicate the prediction for the boundaries among possible stable phases (empty, shell film, or capillary condensation) according to the SFM. Note the existence of a “triple point”. The full circles stand for transitions determined from OP-NLDF calculations. The dashed curve stand for the $E \rightarrow SF$ transition given by the improved SFM.

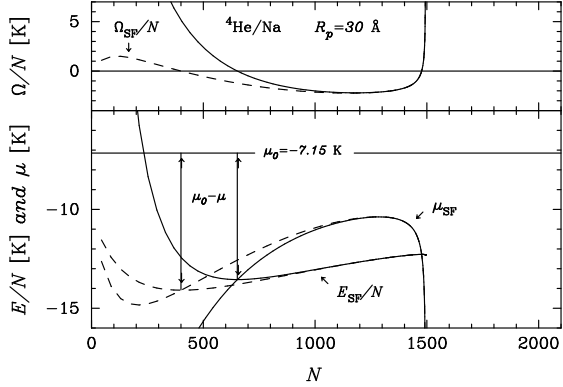


FIG. 5. Energetics of ^4He adsorbed into a Na cavity with $R_p = 30 \text{ \AA}$. *Upper part*: The grand free energy per particle as a function of the number of particles. *Lower part*: Same for the energy per particle and the chemical potential. The solid curves are results of the original SFM while dashed curves are provided by the improved version.

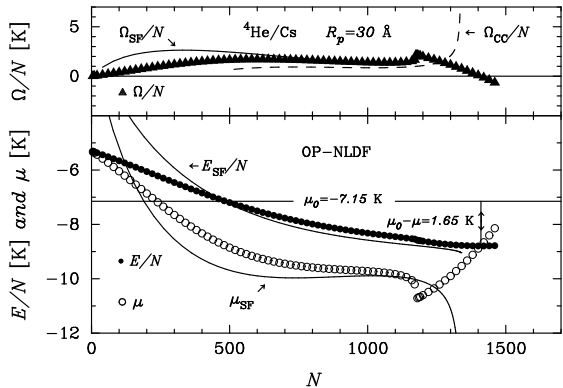


FIG. 6. Energetics of ^4He adsorbed into a Cs cavity with $R_p = 30 \text{ \AA}$. *Upper part*: The grand free energy per particle as a function of the number of particles; *Lower part*: Same for the energy per particle and the chemical potential. The curves indicate results provided by the improved SFM. The symbols stand for values obtained from OP-NLDF calculations.

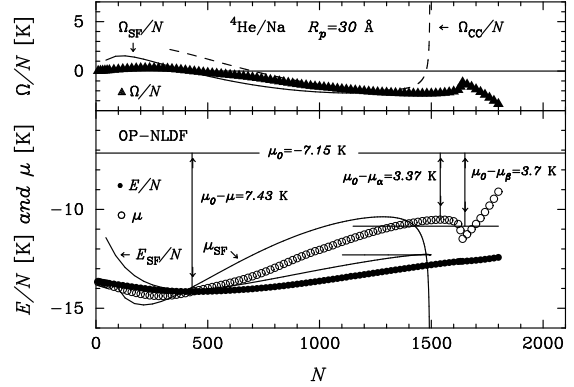


FIG. 7. Same as Fig. 6 for ^4He adsorbed into a Na cavity.

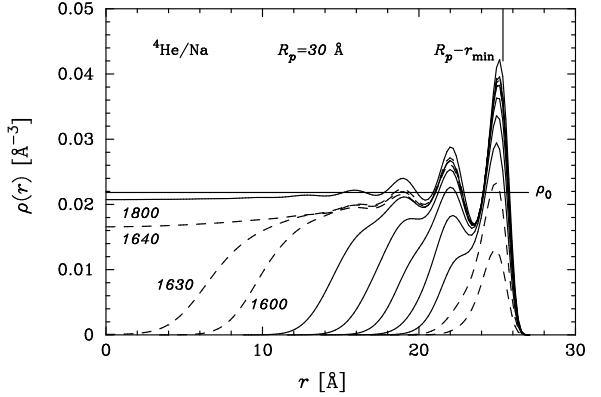


FIG. 8. Density profiles of ^4He adsorbed into a cavity of Na ($R_p = 30 \text{ \AA}$) for $N = 200, 400, 600, 800, 1000, 1200, 1400, 1600, 1630, 1640$, and 1800 . Dashed curves are metastable or unstable solutions.

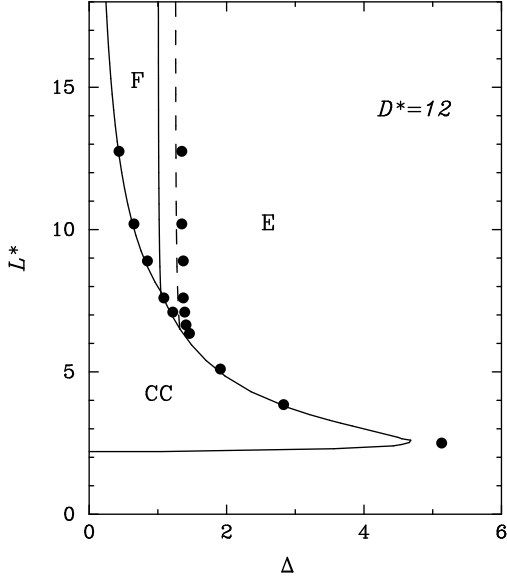


FIG. 9. Reduced phase diagram for ${}^4\text{He}$ confined by two planar walls of Li ($D^* = 12$). Solid curves are SFM predictions and full circles DF results, both of them taken from [4] (see text). The dashed curve shows how much the correction introduced in the present work improves the prediction of the SFM for the $\text{E} \rightarrow \text{F}$ phase transition.

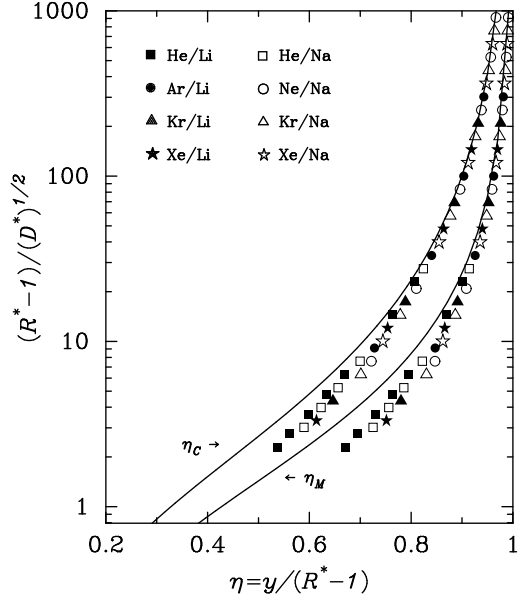


FIG. 10. Nearly universal correspondence of critical values of reduced inner radii η_M and η_C and the dimensionless ratio of effective radius with potential strength $(R^* - 1)/\sqrt{D^*}$ in the single hysteretic loop. The solid curves are asymptotic functions given by Eqs. (3.17) and (3.18).